Sustainable Environment Research

RESEARCH Open Access

Enhanced photocatalytic activity of novel α-Bi_2O_3@g-C_3N_4 composites for the degradation of endocrine-disrupting benzophenone-3 in water under visible light

Abiyu Kerebo Berekute[1,2], Kuo-Pin Yu[1,2*] and Yi-Hsueh Brad Chuang[3]

Abstract

The commonly used benzophenone-3 (BP-3) as ultraviolet filter ingredients is an endocrine-disrupting chemical that has received particular attention owing to its environmental ubiquity, and it poses a threat to aquatic biota and human health. In this study, novel α-Bi_2O_3@g-C_3N_4 nanocomposites with different α-Bi_2O_3 contents and enhanced photocatalytic activity were synthesized by a mixing calcination method. The as-synthesized photocatalysts were characterized by X-ray diffraction, scanning electron microscopy, transmission electron microscopy, X-ray photoelectron spectroscopy, Fourier transform infrared spectroscopy, ultraviolet–visible diffuse reflectance spectroscopy, N_2 adsorption/desorption isotherm analysis, electrochemical impedance spectroscopy, photoluminescence spectroscopy and electron paramagnetic resonance (EPR) spectroscopy. The 1 wt% α-Bi_2O_3@g-C_3N_4 composite exhibited the highest rate constant of 0.42 h^{-1} for photocatalytic degradation of BP-3, which was up to 6.3 times higher than that of g-C_3N_4 (0.07 h^{-1}). The enhanced photocatalytic activity might be due to the enhanced separation of photogenerated electron-hole (e^--h^+) charge pairs and suppression of e^--h^+ recombination. Scavenging experiments suggested that •OH, h^+ and $•O^{2-}$ worked together in the α-Bi_2O_3@g-C_3N_4 photocatalytic process. The EPR spectra demonstrated that the α-Bi_2O_3@g-C_3N_4 composites generated considerably more $•O^{2-}$ and •OH than g-C_3N_4. Finally, cyclic degradation experiments showed the reusability of 1 wt% α-Bi_2O_3@g-C_3N_4 for BP-3 removal.

Keywords: α-Bi_2O_3@g-C_3N_4, Z-scheme heterojunction, Photocatalytic degradation, Ultraviolet filter

1 Introduction

Benzophenone-3 ((2-hydroxy-4-methoxyphenyl) phenylmethanone, BP-3) has received special attention owing to its extensive use, ubiquity, persistence as a contaminant, potential ecotoxicity to aquatic biota and health risks to humans [1, 2]. BP-3 is widely used in cosmetics as a sunscreen ingredient, industrial products and food contact materials; it is commonly used to protect skin from sunburn and materials from possible UV light-induced photochemical degradation [3, 4]. BP-3 may be introduced to aquatic environments directly through human recreational activities such as swimming and indirectly by wastewater treatment plant (WWTP) effluents, which indicates that conventional wastewater treatment processes do not effectively remove BP-3 [5, 6].

Several studies have shown the incomplete removal of BP-3 in conventional WWTPs. For example, Liu et al.

* Correspondence: kpyu03@nycu.edu.tw
[1]International Ph.D Program in Environmental Science and Technology, University System of Taiwan, Taipei 11221, Taiwan
[2]Institute of Environmental and Occupational Health Sciences, National Yang Ming Chiao Tung University, Taipei 11221, Taiwan
Full list of author information is available at the end of the article

reported BP-3 concentrations up to 2086 ng L^{-1} in the influent and up to 153 ng L^{-1} in the effluent, with a removal efficiency of 92% [7], while Wick et al. reported maximum BP-3 concentrations up to 720 ng L^{-1} in the influent [8], and Langford et al. reported maximum BP-3 concentrations up to 1915 ng L^{-1} in the effluent [9]. Similarly, Li et al. reported BP-3 concentrations up to 722 ng L^{-1} in the influent and up to 664 ng L^{-1} in the effluent, with a removal efficiency of only 9%, and Tsui et al. mentioned maximum BP-3 concentrations up to 371.3 ng L^{-1} in the influent and up to 115.8 ng L^{-1} in the effluent, with a removal efficiency of 69% [10, 11].

Advanced oxidation processes (AOPs) involving heterogeneous photocatalysts can effectively remove BP-3 from WWTP effluent. AOPs utilize chemical oxidation based on the *in-situ* generation of free radicals (hydroxyl radical (•OH), superoxide radical ($•O^{2-}$), etc.) that nonselectively react with emerging organic contaminants and are capable of completely degrading them into carbon dioxide and water [12, 13]. Heterogeneous photocatalysts have received particular interest owing to their low cost, nontoxicity, efficiency, lack of secondary pollution and environmental friendliness [14–16]. Wang et al. reported the photocatalytic degradation of BP-3 using PbO@TiO_2 and Sb_2O_3@TiO_2 composites and showed optimal removal efficiencies of up to 87% and 80%, respectively [17]. Zuniga-Benitez et al. reported the photodegradation of BP-3 using UV + TiO_2 treatment with an optimal remnant efficiency of 62% [18].

Recently, metal-free graphitic carbon nitride (g-C_3N_4) has been considered for use as a metal-free π-conjugated photocatalyst with an appropriate bandgap energy (~2.7 eV). It has attracted considerable attention for organic pollutant degradation, hydrogen production, carbon dioxide reduction and atmospheric purification owing to its high thermochemical stability, 2D optical structure, suitable electronic properties and inexpensive synthesis [19, 20]. The more negative conduction potential edge of g-C_3N_4 (-1.22 eV vs. normal hydrogen electrode (NHE)) is enough for the reduction of the adsorbed oxygen (O2/$•O^{2-}$) redox couple (-0.33 eV vs. NHE) to produce $•O^{2-}$. However, the photocatalytic efficiency of pristine g-C_3N_4 catalysts is low because of the fast recombination of photoinduced e^- and h^+, limited delocalized conductivity, low quantum efficiency and narrow visible light absorption range [21, 22]. Consequently, to improve the photocatalytic performance, the application of various strategies, such as heterojunction formation, surface modification, metal or anion doping and use of dye-sensitized photocatalysts, is important. Among the aforementioned strategies, heterojunction formation efficiently suppresses charge carrier recombination, leads to excellent e^- and h^+ separation and promotes the redox capacity of photogenerated carriers, thus enhancing the photocatalytic performance of the materials [23–25].

Herein, two or more semiconductors with appropriate bandgap energies are combined to fabricate type II heterojunction photocatalysts. Such photocatalysts can be formed by photogenerated electrons being transferred from the conduction band of photosystem I (PSI) to the valence band (VB) of photosystem II (PSII), while the hole is transferred in the opposite direction due to the potential difference between the conduction band and the VB edges. This potential difference improves the charge separation efficiency and suppresses recombination, which is favorable for photocatalytic performance. However, these merits are at the expense of the reduction abilities of PSI and oxidation abilities of PSII [26–28].

Regarding a Z-scheme photocatalytic system, the photoexcited electrons in the conduction band of PSII, which stem from visible light irradiation, may recombine with holes in the VB of PSI. Therefore, the conduction band edge of PSII should be lower than that of PSI, and the VB edge of PSI should be higher than that of PSII. Thus, strong oxidative holes and reductive electrons can be generated in the two different bands, thereby resulting in enhanced photocatalytic activity [25, 29].

Currently, a number of bismuth-containing semiconductors, such as bismuth oxide (Bi_2O_3), $BiVO_4$, Bi_2WO_6 and BiOX (X = Cl, Br, I), are available. As a preeminent semiconductor, Bi_2O_3, which has a band gap of ~2.8 eV, has received increasing attention owing to its nontoxicity, thermal stability, environmental friendliness, outstanding visible light absorption and strong oxidation when used as a photocatalyst. It has been reported that Bi_2O_3 exhibits six polymorphs, α, β, ϒ, δ, ε and ω phases. Among them, α-Bi_2O_3 has a monoclinic structure and is stable under ambient pressure and temperature conditions [27, 30, 31]. The more positive valence potential edge of α-Bi_2O_3 (2.89 eV vs. NHE) is enough for the oxidation of the water H_2O/•OH redox couple (2.72 eV vs. NHE) and hydroxyl ion OH^-/•OH redox couple (2.40 eV vs. NHE) to produce •OH radicals. Therefore, considering the matching band gap alignments and appropriate band edge potentials of semiconductors, α-Bi_2O_3 is a promising candidate for integration with g-C_3N_4 to construct a direct Z-scheme heterojunction.

In the present study, we synthesized α-Bi_2O_3@g-C_3N_4 photocatalysts with different weight percentages of α-Bi_2O_3 through a mixing-calcination method. The objective of our study was to investigate the photocatalytic activity of the as-synthesized samples for the degradation of BP-3 and the effects of α-Bi_2O_3 doping on the photocatalytic properties of g-C_3N_4 catalysts. The as-synthesized samples were characterized by X-ray diffraction (XRD), scanning electron microscopy (SEM), transmission electron microscopy (TEM), X-ray

photoelectron spectroscopy (XPS), Fourier transform infrared (FT-IR) spectroscopy, (ultraviolet–visible diffuse reflectance spectroscopy (UV-Vis DRS), N_2 adsorption/desorption isotherm analysis, electrochemical impedance spectroscopy (EIS) and photoluminescence (PL) spectroscopy. Furthermore, a possible reaction mechanism was proposed based on the energy band positions and electron paramagnetic resonance (EPR) spectroscopy and trapping experimental findings. Finally, the reusability of the best-performing photocatalyst in the photocatalytic process was also investigated.

2 Materials and methods

2.1 Chemicals

All chemicals, including melamine powder ($C_3H_6N_6$, 99.5%), bismuth (III) nitrate pentahydrate (Bi $(NO_3)_3{\cdot}5H_2O$), isopropanol (IPA, C_3H_8O, 99.9%), superoxide dismutase (SOD, 99%), ammonium oxalate (AO, 99.9%), BP-3 (98%), barium sulfate ($BaSO_4$, 99%), and methanol (CH_3OH, 99.9%), were purchased from Sigma–Aldrich. All reagents and precursors were used as received without further purification, and deionized water was used in this study.

2.2 Synthesis of the α-Bi_2O_3@g-C_3N_4 photocatalyst

g-C_3N_4 was synthesized according to a previously reported method [32]. In a typical synthesis procedure, 5 g of melamine ($C_3H_6N_6$) was placed in a crucible with a cover. The crucible was heated to 520 °C under nitrogen in a tube furnace at a heating rate of 10 °C min^{-1} and held for 2 h. Further deammoniation treatment was performed at 540 °C for 2 h. After the reaction, the crucible was cooled to room temperature. The yellow product was collected and ground into a powder.

α-Bi_2O_3 was synthesized according to a previously reported method [33]. Bismuth (III) nitrate pentahydrate (Bi $(NO_3)_3{\cdot}5H_2O$) was dried at 60 °C for 2 h to obtain bismuth (III) nitrate (Bi $(NO_3)_3$) powder without crystal water. Thereafter, 5 g of Bi $(NO_3)_3$ was placed in a crucible, which was first heated in a tube furnace with a nitrogen atmosphere at 600 °C for 2 h and further heated at 620 °C for 2 h at a heating rate of 10 °C min^{-1}. After the reaction, the crucible was allowed to cool naturally to room temperature. The yellow product was collected and ground into a powder.

α-Bi_2O_3@g-C_3N_4 composites were synthesized according to a previously reported method [34] with some modification. In detail, 10 g of $C_3H_6N_6$ was first dissolved in 50 mL of a methanol solution by adding different amounts of Bi $(NO_3)_3$. The suspension was continuously stirred for 2 h at room temperature and then transferred to a vacuum drying oven at 80 °C for 24 h. Next, the white precursor mixture was ground and added to a crucible with a cover. Finally, the precursor mixture was heated in a tube furnace with a nitrogen atmosphere for 2 h, reaching a temperature of 520 °C at a heating rate of 10 °C min^{-1}. Further treatment was performed at 540 °C for 2 h. When 0.05, 0.1, 0.3 and 0.5 g Bi $(NO_3)_3$ were used, the obtained yellow solids were ground into powders and labeled 0.5 wt% α-Bi_2O_3@g-C_3N_4, 1 wt% α-Bi_2O_3@g-C_3N_4, 3 wt% α-Bi_2O_3@g-C_3N_4 and 5 wt% α-Bi_2O_3@g-C_3N_4. A schematic illustration of the synthesis method is shown in Fig. S1 of Supplemental Materials.

2.3 Material characterization

2.3.1 Physicochemical characterization

Physicochemical characterization of the as-synthesized samples was obtained using SEM, SEM-EDS, TEM, XRD, XPS and FT-IR spectroscopy, and N_2 adsorption and desorption isotherms. The crystal structure and phase composition of the as-synthesized samples were studied by XRD using a Bruker D2 Phaser diffractometer (Japan). The X-ray powder diffractometer was operated at 10 kV and used a Cu Kα radiation source with a wavelength of 1.5406 Å. The morphologies and elemental composition of the samples were studied by field-emission SEM (FE-SEM; JEOL JSM-7600F, Tokyo, Japan), in which the microscope was equipped with energy dispersive spectroscopy (EDS) and operated at an accelerating voltage of 15 kV, and TEM (JEOL JEM 1400Plus electron microscope, Tokyo, Japan). XPS measurements were performed with a Thermo VG Scientific XPS (ESCALAB 250, England). Moreover, all the binding energies were calibrated with respect to the C 1s peak of the adventitious carbon at 284.9 eV. FT-IR spectra of the as-synthesized samples were recorded on a JASCO-4200 spectrometer at room temperature with KBr as a reference sample. N_2 adsorption and desorption isotherm curves were obtained with a Micromeritics system at 77.35 K (Autosorb-Iq-MP, Quantachrome Instruments).

2.3.2 Photoelectrochemical characterization

Photoelectrochemical characterization of the as-synthesized samples was obtained using UV-Vis spectrophotometry, PL spectroscopy, EIS analysis and EPR spectroscopy. The absorbance, diffuse reflectance spectra and optical bandgap of each sample were assessed using a UV-Vis spectrophotometer (JASCD 760) with $BaSO_4$ as a reference sample. PL emission spectra were measured at room temperature on a JASCD FB-8500 fluorescence spectrophotometer. EIS was performed using an Autolab PGSTAT302N electrochemical test system (Metrohm Autolab B.V., Netherlands). EIS was performed for the as-synthesized samples with a standard three-electrode system that utilized Ag/AgCl and platinum strips as the reference and counter electrodes,

respectively. The working electrode was prepared by mixing 8 mg of the as-synthesized samples with 1 mg of polyvinylidene fluoride and 1 mg of carbon black, and then, 100 μL n-methyl-2-pyrrolidone was added. Thereafter, the slurry was coated on a 1 × 3 cm piece of nickel foam and dried at 60 °C for 12 h in a vacuum oven. The EIS spectra were recorded from 0.1 to 100 kHz at a current amplitude of 10 mV and with a 0.5 M Na_2SO_4 aqueous solution as the electrolyte.

2.3.3 The measurement of reactive oxygen species (ROS)

A Bruker EPR spectrometer was used to measure the ROS in the presence of 5,5-dimethyl-1-pyrroline N-oxide (DMPO) to further verify the generation of ROS in the photocatalytic systems. The samples were prepared as follows: 20 mg of the as-synthesized samples was dispersed in 1 mL of deionized water, and then, 80 μL of DMPO was introduced with a 3 min ultrasonic treatment, which was used to trap hydroxyl radicals (DMPO-•OH). The superoxide radicals (DMPO-•O^{2-}) were determined by the same process except that the deionized water was replaced with methanol.

2.4 Photocatalytic degradation of BP-3

The photocatalytic activities of the as-synthesized g-C_3N_4 and α-Bi_2O_3@g-C_3N_4 composites were evaluated by using BP-3 as the organic contaminant. Briefly, the process was performed by dispersing 0.15 g of the as-prepared sample into 100 mL of a BP-3 solution at an initial concentration of 2 mg L^{-1} and with the pH of the pristine solution. The formed suspension was stirred in the dark for half an hour to establish an adsorption/desorption equilibrium. Next, the solution was exposed to 24 W m^{-2} visible light irradiation (Philips CLEO HPA 400S, λ > 420 nm), and the suspension was continuously stirred magnetically at 450 rpm. As an illustration, the apparatus used for the photocatalytic experiment is presented in Fig. S2. During the photodegradation process, a 4 mL aliquot was removed at a predetermined time, and the complete removal of the catalyst particles was achieved by centrifugation and filtration through a 0.2-μm Millipore filter. The supernatant was analyzed by UV-Vis spectrophotometry to monitor both the absorbance and absorption spectra of the remaining BP-3. To further confirm the photodegradation of BP-3, aliquots were collected and analyzed using high-performance liquid chromatography (HPLC). Eq. (1) was used to determine the removal efficiency (η%):

$$\eta(\%) = \frac{C_i - C_f}{C_i} \times 100 \quad (1)$$

where C_i is the initial BP-3 concentration in mg L^{-1} before irradiation and C_f is the BP-3 concentration in mg L^{-1} after illumination time t.

2.5 Influence of ROS scavengers on the photocatalytic process

An active species trapping experiment was performed by using the 1 wt% α-Bi_2O_3@g-C_3N_4 catalyst for the photodegradation of BP-3. The degradation process was observed by adding different active species quenchers. To do this, AO (5 mg), SOD (5 mg) and IPA (5 mL) were chosen as the quenchers of h^+, •O_2^- and •OH, respectively. The utilized method was similar to that of the previous photocatalytic activity test except when treated with the respective quenchers in the presence of BP-3.

2.6 Photocatalyst reusability test

To assess the reusability of the photocatalyst, 0.15 g of the 1 wt% α-Bi_2O_3@g-C_3N_4 catalyst was dispersed in 100 mL of a 2 mg L^{-1} BP-3 solution and then illuminated for 300 min to complete the first BP-3 degradation cycle. Thereafter, the used catalysts in solution were centrifuged, repeatedly washed with water and alcohol, dried at 60 °C for 12 h in a vacuum drying oven, and then used again in the next experiment. The same procedure was repeated for all the remaining cycles.

3 Results and discussion

3.1 Characterization of the catalysts

The surface morphologies of the as-synthesized g-C_3N_4, α-Bi_2O_3 and 1 wt% α-Bi_2O_3@g-C_3N_4 composite samples were studied by FE-SEM. According to Fig. 1a, g-C_3N_4 exhibits an aggregated structure, and clearly, the surface structure of α-Bi_2O_3 in Fig. 1b exhibits thin sheet hierarchical microspheres. However, in Fig. 1c, Figs. S3a, S4a and S5a of the 1, 0.5, 3 and 5 wt% α-Bi_2O_3@g-C_3N_4 composite samples show the aggregated g-C_3N_4 structure covered by the thin sheet hierarchical microspheres of the α-Bi_2O_3 particles, confirming the formation of the α-Bi_2O_3@g-C_3N_4 composites [27, 35]. Small pores were observed on the surface structure of the α-Bi_2O_3@g-C_3N_4 composite; these pores might be due to the release of small molecular gases, specifically NO_2 and H_2O, during the mixing-calcination process. The elemental compositions of the 1, 0.5, 3 and 5 wt% α-Bi_2O_3@g-C_3N_4 composites were determined by EDS, and the results are shown in Fig. 1d, Figs. S3b, S4b and S5b. The EDS spectra reveal that the as-synthesized samples contain carbon (C), nitrogen (N), bismuth (Bi), and oxygen (O). Therefore, the EDS results confirm the presence of Bi, O, C, and N in the 1, 0.5, 3 and 5 wt% α-Bi_2O_3@g-C_3N_4 composites, further indicating the presence of both α-Bi_2O_3 and g-C_3N_4. Additionally, the elemental maps of the as-synthesized samples in Fig. 2a-d, Figs. S6, S7 and S8 confirm the presence of C, N, Bi, and O in the 1, 0.5, 3 and 5 wt% α-Bi_2O_3@g-C_3N_4 composites, respectively.

TEM was used for structural analysis and microstructural characterization of the as-synthesized g-C_3N_4, α-

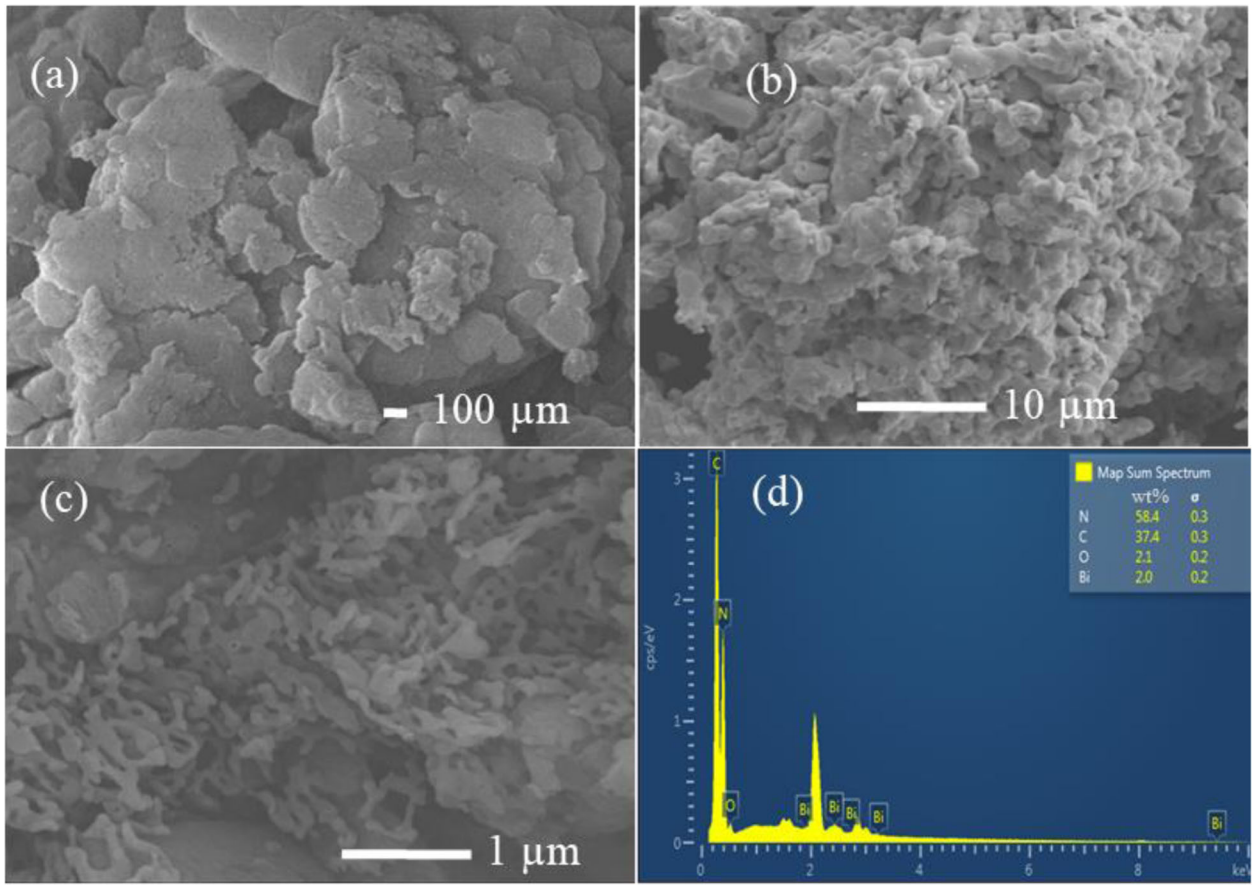

Fig. 1 SEM images of (**a**) g-C_3N_4, (**b**) α-Bi_2O_3 and (**c**) 1 wt% α-Bi_2O_3@g-C_3N_4 and (**d**) EDS spectra of 1 wt% α-Bi_2O_3@g-C_3N_4

Bi_2O_3 and 1 wt% α-Bi_2O_3@g-C_3N_4 composite samples. Figure 3a and b shows that the pure g-C_3N_4 sample displays a typical smooth surface with a layered sheet structure [20], and the pure α-Bi_2O_3 sample shows a dark image of nanoparticles, as demonstrated in Fig. 3c. The deposition of α-Bi_2O_3 on the surface of g-C_3N_4 is clearly observed in the TEM images of 1 wt% α-Bi_2O_3@g-C_3N_4, as shown in Fig. 3e. Numerous dark, particle-like structures are observed on the surface of g-C_3N_4. Consequently, the dark particles can be assigned to α-Bi_2O_3, and the gray part and layered sheet are assigned to g-C_3N_4. Since Bi has a higher atomic mass than C and N, the electron beam can penetrate g-C_3N_4 more easily than α-Bi_2O_3. High-resolution TEM was further performed to investigate the d-spacing of the as-synthesized catalysts, and the results are displayed in Fig. 3b, d and f. The 0.376 nm d-spacing of the lattice fringes corresponds to the (002) lattice plane of g-C_3N_4 (Fig. 3b), while the 0.401 nm d-spacing of the lattice fringes corresponds to the (021) lattice plane of α-Bi_2O_3 (Fig. 3d). In addition, Fig. 3f displays the presence of α-Bi_2O_3 and g-C_3N_4 phases and an interplanar spacing of 0.406 nm, which correspond to the (021) crystal plane of α-Bi_2O_3, further confirming the formation of heterojunctions in the as-synthesized sample.

The XRD patterns of the as-synthesized g-C_3N_4, α-Bi_2O_3, 0.5 wt% α-Bi_2O_3@g-C_3N_4, 1 wt% α-Bi_2O_3@g-C_3N_4, 3 wt% α-Bi_2O_3@g-C_3N_4 and 5 wt% α-Bi_2O_3@g-C_3N_4 catalysts are shown in Fig. 4a. The characteristic peaks of the g-C_3N_4 sample are indexed to the corresponding orthorhombic phase (PDF #89-8491) with lattice parameters of a = 4.048 Å, b = 4.885 Å and c = 6.495 Å. The g-C_3N_4 catalyst shows two diffraction peaks at 2θ = 13.62 and 27.44°, which can be indexed as the (001) and (002) planes, respectively. The weak peak at 13.62° corresponds to an interlayer d-spacing of 0.649 nm, which is related to the order of the tri-s-triazine in-plane structural repeating unit, and the strong peak at 27.44°, which corresponds to an interlayer d-spacing of 0.367 nm, is attributed to the long-range interlayer stacking of aromatic systems and/or graphitic sheets [36, 37]. The peaks of the α-Bi_2O_3 sample are related to the corresponding monoclinic phase (PDF #02-0498) with lattice parameters of a = 5.830 Å, b = 8.140 Å and c = 7.480 Å. The diffraction peaks located at 2θ = 26.03, 27.59, 33.53 and 46.53° are attributed to the (002), (121),

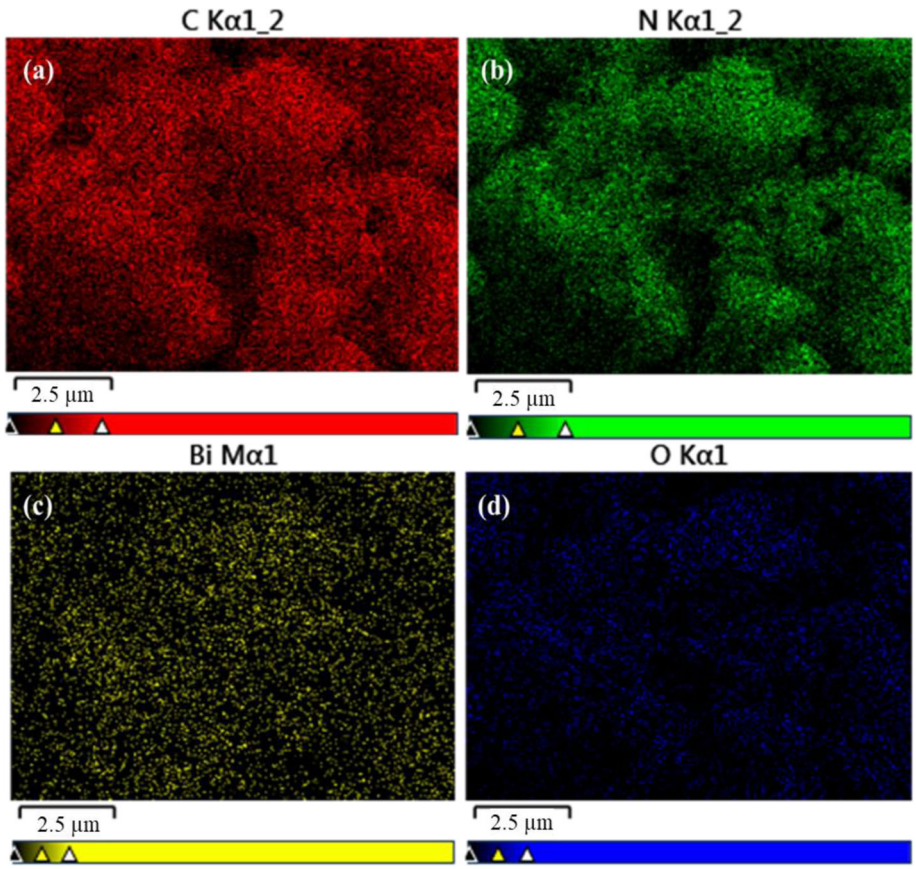

Fig. 2 EDS elemental mapping (**a**) C, (**b**) N, (**c**) Bi and (**d**) O of 1 wt% α-Bi_2O_3@g-C_3N_4

(202) and (041) planes, respectively. The peaks of α-Bi_2O_3, especially the peak at 27.59°, are very sharp, which suggests good crystallinity. The intensity of the XRD peaks of the α-Bi_2O_3@g-C_3N_4 composites decreases as the α-Bi_2O_3 content increases from 0.5 to 5 wt%, and the peak of α-Bi_2O_3 that is ascribed to the monoclinic phase is not identified. Therefore, the α-Bi_2O_3 particles are confirmed to be homogeneously dispersed on the surface of g-C_3N_4, which results in a significant decrease in the intensity of the (002) peaks of the composite catalysts. In addition, no new diffraction peaks are observed in the composite, which confirms that the composite contains only g-C_3N_4 and α-Bi_2O_3 [38, 39]. The crystallite sizes of g-C_3N_4, α-Bi_2O_3 and the 1 wt% α-Bi_2O_3@g-C_3N_4 composite are estimated to be 6.73, 14.18 and 4.47 nm, respectively.

The chemical bonding of the as-synthesized g-C_3N_4, α-Bi_2O_3 and α-Bi_2O_3@g-C_3N_4 composites with different weight percentages of α-Bi_2O_3 was investigated by FT-IR spectroscopy. The spectra are depicted in Fig. 4b. Regarding g-C_3N_4, the sharp peak centered at 808 cm^{-1} can be assigned to the out-of-plane bending modes of the s-triazine units [23]. Moreover, the peaks located at 1560, 1412, 1321 and 1242 cm^{-1} correspond to aromatic C–N stretching vibrations, whereas the peak located at 1641 cm^{-1} is assigned to the C=N stretching vibration mode [40]. Additionally, the broad peak centered at 3000-3300 cm^{-1} is associated with the stretching vibration mode of NH_2 or N-H groups, and the bending vibration of the O-H band resembles that of adsorbed water [37, 41]. The peak of α-Bi_2O_3 located at approximately 520 cm^{-1} corresponds to the typical stretching vibration mode of the Bi–O bands of BiO_6 units [42]. Regarding the four α-Bi_2O_3@g-C_3N_4 composites, the peak of α-Bi_2O_3 centered at 520 cm^{-1} is not observed in all composite samples, which might be due to its low content and weak vibrations. Similar trends have been reported by Huang et al. [43] and Wang et al. [44] regarding CeO_2@g-C_3N_4 and sulfur-doped@g-C_3N_4, respectively. However, strong peak intensities from g-C_3N_4 are observed in the 1240-1640 cm^{-1} region when the α-Bi_2O_3 content in the composites is increased from 0.5 to 5 wt%.

The surface chemical compositions of g-C_3N_4, α-Bi_2O_3 and the 1 wt% α-Bi_2O_3@g-C_3N_4 composite were analyzed by XPS. Figure S9a shows the full survey XPS spectra of α-Bi_2O_3, g-C_3N_4 and 1 wt% α-Bi_2O_3@g-C_3N_4. Clearly, Bi 4f, O 1s, C 1s and N 1s signals are observed for all samples. Figure 5a-d depicts the Bi 4f, O 1s, C 1s

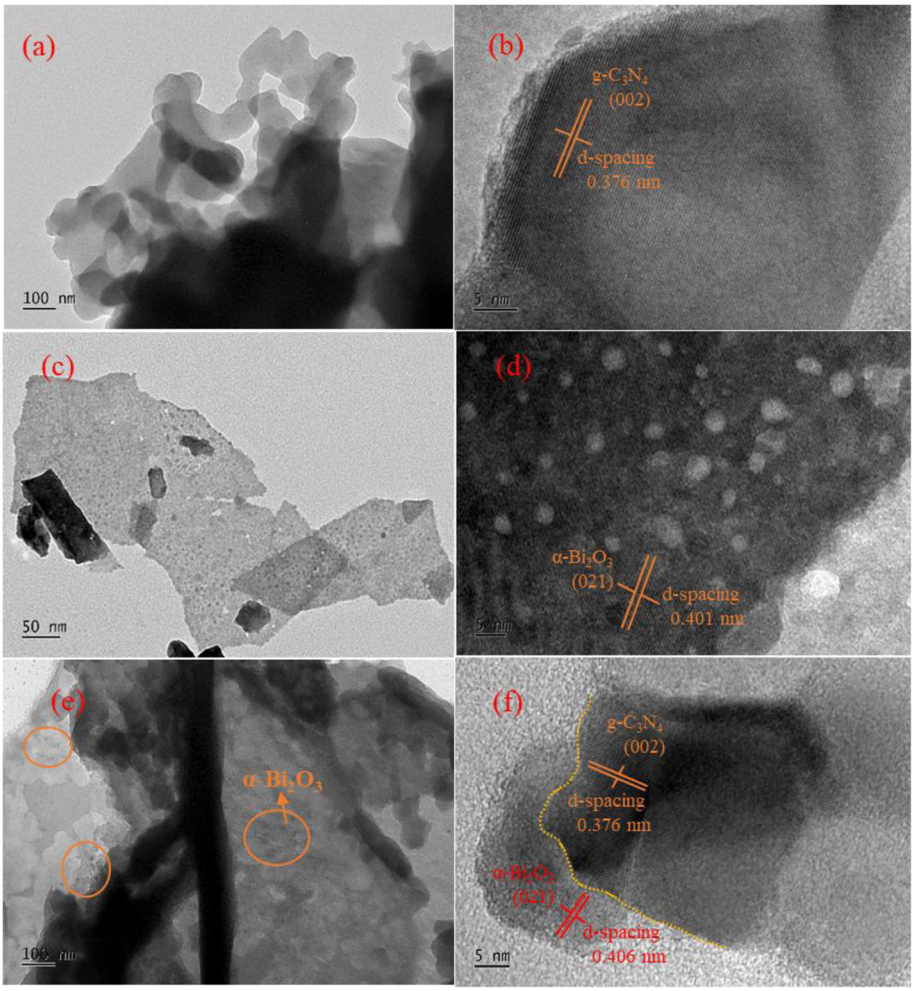

Fig. 3 TEM and HRTEM images of (**a** and **b**) g-C_3N_4, (**c** and **d**) α-Bi_2O_3 and (**e** and **f**) 1 wt% α-Bi_2O_3@g-C_3N_4

and N 1s XPS spectra of α-Bi_2O_3, g-C_3N_4 and 1 wt% α-Bi_2O_3@g-C_3N_4. Figure 5a shows the Bi 4f high-resolution spectra of α-Bi_2O_3 and 1 wt% α-Bi_2O_3@g-C_3N_4. The two peaks centered at 159.3 eV and 164.3 eV represent the $4f_{7/2}$ and $4f_{5/2}$ orbitals of trivalent Bi (Bi^{3+}) in α-Bi_2O_3, respectively [33]. However, the binding energies of the Bi $4f_{7/2}$ and Bi $4f_{5/2}$ orbitals in 1 wt% α-Bi_2O_3@g-C_3N_4 shift to 158.3 eV and 163.3 eV, respectively, which indicates the formation of a heterojunction between g-C_3N_4 and α-Bi_2O_3 in the composite [40]. Figure 5b shows two strong peaks at 529.9 eV and 530.4 eV, which are the binding energies of the O 1s core level; the former peak is attributed to the lattice O^{2-} species of the Bi-O bonds, while the latter peak can be assigned to surface-absorbed hydroxyl oxygen [43]. Compared with that of α-Bi_2O_3, the O 1s signal in of 1 wt% α-Bi_2O_3@g-C_3N_4 shows a positive shift, which also confirms the formation of a heterojunction between g-C_3N_4 and α-Bi_2O_3 in the composite.

The C 1s spectrum shown in Fig. 5c shows two peaks and binding energies at 284.9 eV and 288.6 eV, which correspond to the carbon species adsorbed on the sample surface from the instrument and the sp2-hybridized bonded carbon in the heterocyclic aromatic ring (N–C=N) of the g-C_3N_4 lattice, respectively [45]. As shown in Fig. 5c, the signal in the C 1s spectrum shifts to a lower binding energy after α-Bi_2O_3 loading, which further confirms the formation of heterojunctions. The binding energy of the adventitious carbon peak (284.9 eV) does not change after heterojunction formation.

The N 1s spectrum of g-C_3N_4 in Fig. 5d shows three peaks centered at 398.5, 399.3 and 399.5 eV, which are assigned to the tertiary N bonded to carbon atoms in the form of N-$(C)_3$ units, the sp^2-hybridized aromatic N atoms bonded to carbon in the form of C-N=C, and amino groups with a hydrogen atom (C-N-H) and charging effects, respectively [19, 37]. As shown in Fig. 5d, the N 1s binding energy of 1 wt% α-Bi_2O_3@g-C_3N_4 exhibits a blueshift, which also suggests a possible

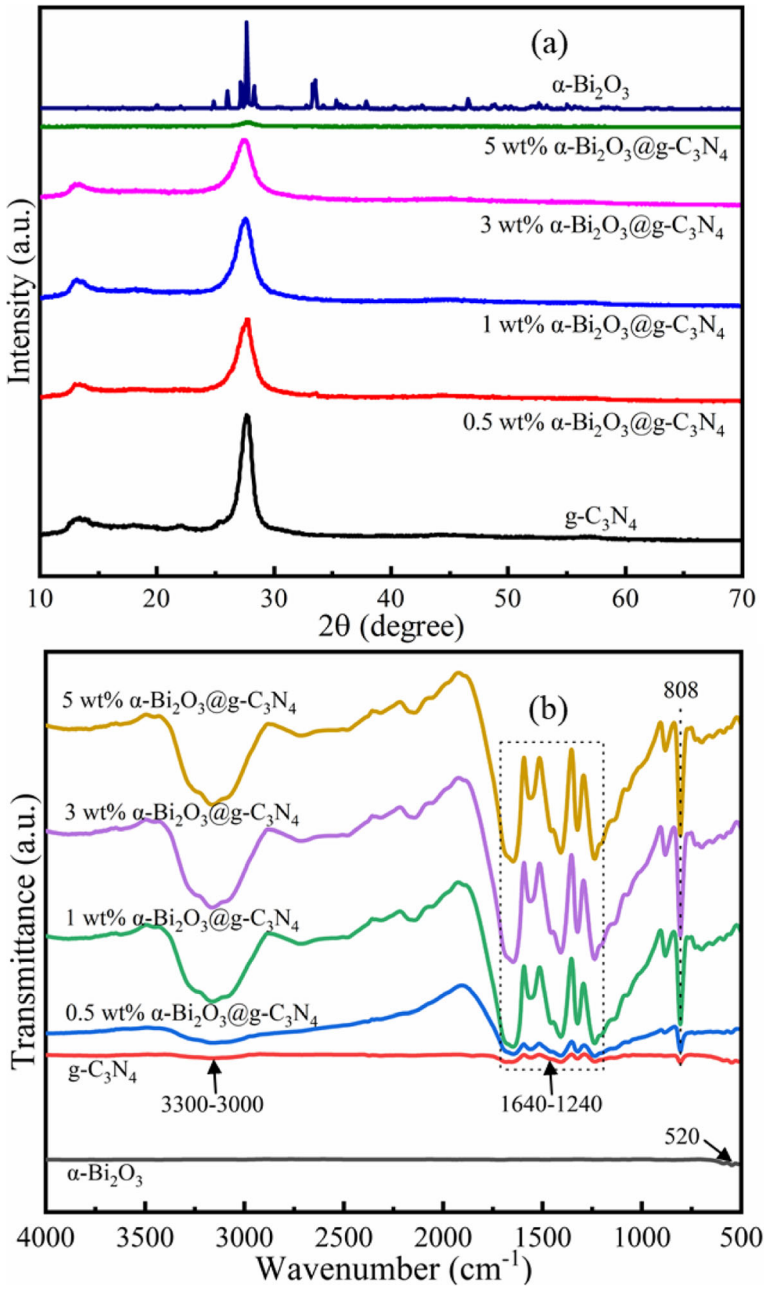

Fig. 4 (**a**) XRD patterns and (**b**) FT-IR spectra of g-C_3N_4, α-Bi_2O_3 and the α-Bi_2O_3@g-C_3N_4 composites

interaction between g-C_3N_4 and α-Bi_2O_3 in the composite. Generally, this kind of interaction promotes charge carrier separation and interparticle electron transfer, leading to the enhanced photocatalytic performance of 1 wt% α-Bi_2O_3@g-C_3N_4.

To investigate the surface physicochemical properties of the as-synthesized samples with respect to the surface area and pore size distribution, nitrogen adsorption-desorption isotherms were obtained. As shown in Fig. S9c, g-C_3N_4, α-Bi_2O_3 and the α-Bi_2O_3@g-C_3N_4 composites exhibit type IV isotherms with a type H3 hysteresis loop, as defined by International Union of Pure and Applied Chemistry; these results are characteristic of slit-like mesoporous materials [46].

Furthermore, the BET surface areas, pore volumes and pore diameters of the g-C_3N_4, α-Bi_2O_3, 0.5 wt% α-Bi_2O_3@g-C_3N_4, 1 wt% α-Bi_2O_3@g-C_3N_4, 3 wt% α-Bi_2O_3@g-C_3N_4 and 5 wt% α-Bi_2O_3@g-C_3N_4 samples are summarized in Table 1. The results suggest that α-Bi_2O_3 loading reduces the BET surface area of the composite

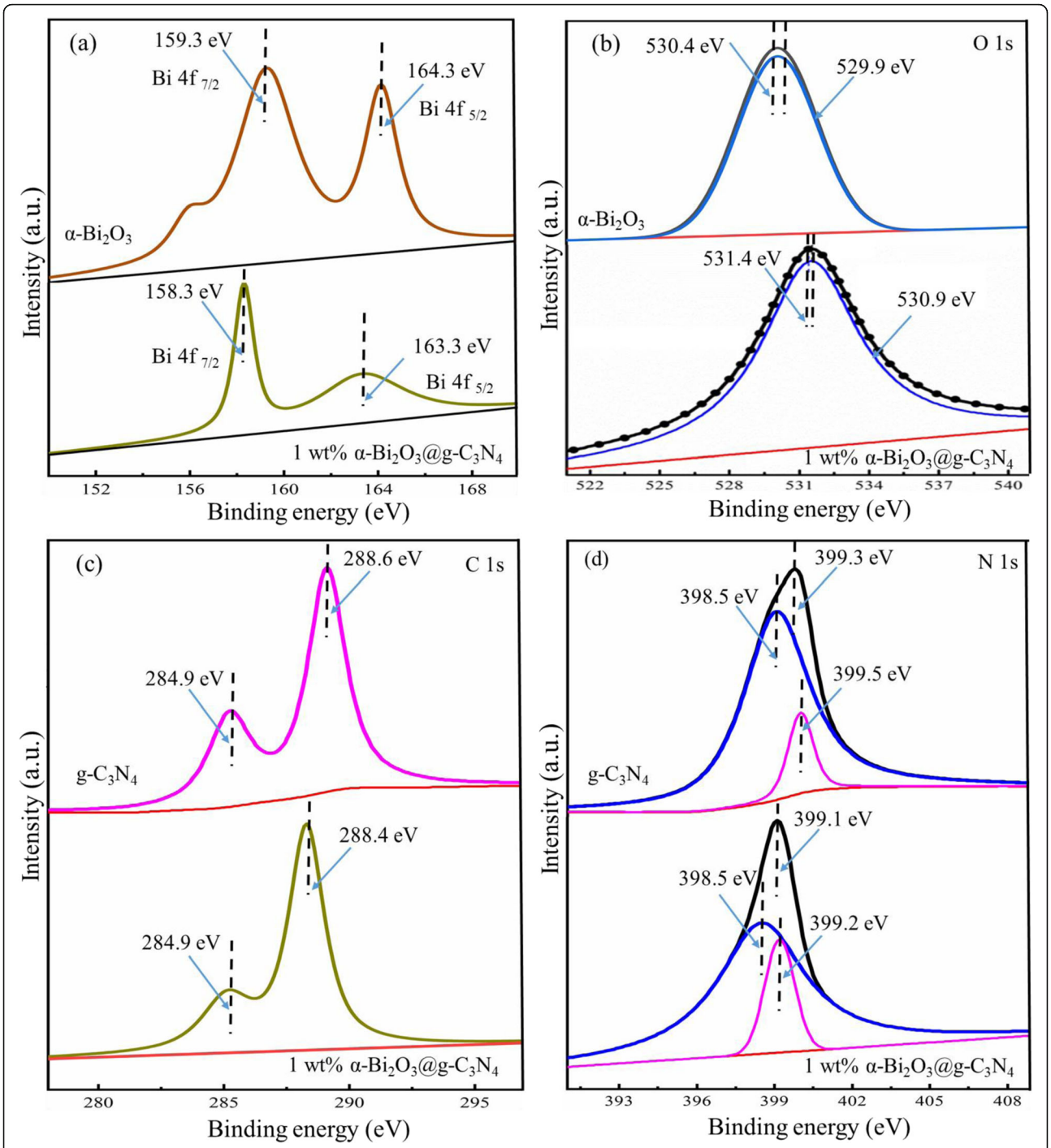

Fig. 5 High-resolution XPS spectra of g-C_3N_4, α-Bi_2O_3 and 1 wt% α-Bi_2O_3@g-C_3N_4 (**a**) Bi 4f; (**b**) O 1s; (**c**) C 1s; (**d**) N 1s

samples, possibly due to the particle aggregation that occurs on the surface of g-C_3N_4. The BET surface area of 1 wt% α-Bi_2O_3@g-C_3N_4 is larger than that of 0.5 wt% α-Bi_2O_3@g-C_3N_4, 3 wt% α-Bi_2O_3@g-C_3N_4 and 5 wt% α-Bi_2O_3@g-C_3N_4. This phenomenon could be due to the different pore size distributions of the as-synthesized samples, as shown in Fig. S9d. Therefore, the high BET surface area of 1 wt% α-Bi_2O_3@g-C_3N_4 offers the possibility for efficient diffusion of the pollutant on the catalyst surface, which is beneficial for the photocatalytic reaction [45].

3.2 UV-Vis DRS analysis

The optical properties of the as-synthesized samples were measured by UV-Vis DRS. Figure 6a shows the

Table 1 BET surface areas, pore diameters and pore volumes of the as-synthesized samples

Photocatalyst	S_{BET} (m^2 g^{-1})[a]	Pore diameter (nm)[b]	Pore volume (cm^3 g^{-1})[c]
g-C_3N_4	18.1	1.909	0.074
0.5 wt% α-Bi_2O_3@g-C_3N_4	8.4	1.912	0.048
1 wt% α-Bi_2O_3@g-C_3N_4	17.1	1.908	0.066
3 wt% α-Bi_2O_3@g-C_3N_4	11.1	1.909	0.045
5 wt% α-Bi_2O_3@g-C_3N_4	12.7	1.910	0.044
α-Bi_2O_3	7.4	1.532	0.013

[a] BET specific surface area; [b] pore diameter calculated from the desorption branch of the isotherm using the BJH method; [c] total pore volume measured at P/P_0 = 0.99.

UV-Vis DRS spectra of the as-synthesized samples. The Kubelka-Munk equation (Eq. (2)) is used to calculate the optical bandgap energy of semiconductors [47].

$$\alpha h\nu = A\left(h\nu - E_g\right)^{n/2} \tag{2}$$

where α is the absorption coefficient, h is Planck's constant, ν is the light frequency, A is a constant, E_g is the bandgap energy, and n depends on the nature of the transition in a semiconductor (n = 1 for a direct transition and n = 4 for an indirect transition). The intrinsic E_g values were determined by extrapolating the steepest portion of $(\alpha h\nu)^2$ = 0. The light absorption onset edges of g-C_3N_4, α-Bi_2O_3, 0.5 wt% α-Bi_2O_3@g-C_3N_4, 1 wt% α-Bi_2O_3@g-C_3N_4, 3 wt% α-Bi_2O_3@g-C_3N_4 and 5 wt% α-Bi_2O_3@g-C_3N_4 are approximately 450, 437, 453, 455, 459 and 463 nm, respectively, with E_g values of 2.72, 2.8, 2.70, 2.69, 2.66 and 2.64 eV, respectively (Fig. 6b). The absorption spectra of the α-Bi_2O_3@g-C_3N_4 composites show a slight redshift, which is triggered by the α-Bi_2O_3 doped on the porous surface of g-C_3N_4, confirming the formation of heterojunctions between g-C_3N_4 and α-Bi_2O_3. Figure S9b shows that the optical bandgaps of the α-Bi_2O_3@g-C_3N_4 composites linearly decrease with an increasing concentration of α-Bi_2O_3, which may result from the interaction between g-C_3N_4 and α-Bi_2O_3.

3.3 Photocatalytic activity evaluation

Figure S10a shows that the time-dependent absorption spectra obtained for the direct photolysis of BP-3 are unchanged without the addition of a catalyst. This result confirms that BP-3 is highly photostable owing to the strong intramolecular hydrogen bonds between the carbonyl oxygen and hydrogen atoms of the ortho hydroxyl group [48]. However, BP-3 can undergo rapid photocatalytic decomposition over α-Bi_2O_3@g-C_3N_4 composites, as demonstrated in Figs. S10 and S11. Figures S11b, 11c, 11d, 10b and 10c show the photocatalytic degradation of BP-3 by g-C_3N_4 and the 0.5, 1, 3 and 5 wt% α-Bi_2O_3@g-C_3N_4 catalysts, respectively.

Figure 7a shows that approximately 20% of BP-3 is removed by adsorption in the dark, and the photocatalytic activity of pristine g-C_3N_4 is relatively low, with only 55% of BP-3 being photocatalytically degraded. However, the α-Bi_2O_3@g-C_3N_4 composites show higher photocatalytic activity than pristine g-C_3N_4, and the 1 wt% α-Bi_2O_3@g-C_3N_4 composite shows the optimal removal efficiency, decomposing 92% of BP-3. Notably, the photocatalytic efficiencies for the photodegradation of BP-3 decrease by 5 and 14% for 3 wt% α-Bi_2O_3@g-C_3N_4 and 5 wt% α-Bi_2O_3@g-C_3N_4, respectively. This phenomenon may be due to the excess loading of α-Bi_2O_3 decreasing the BET areas and the photoinduced charge transfer efficiency (as shown in the EIS results), thus leading to poor photocatalytic performance.

The Langmuir–Hinshelwood (L–H) kinetic model equation (Eq. (3)) is widely used to describe photocatalytic kinetics:

$$r = -\frac{dC}{dt} = k_{L\text{-}H}\frac{K_{L\text{-}H}C}{1 + K_{L\text{-}H}C} \tag{3}$$

where r is the photocatalytic reaction rate, $k_{L\text{-}H}$ is the reaction rate constant, $K_{L\text{-}H}$ is the adsorption constant of BP-3 on the surface of a photocatalyst, and C is the concentration of BP-3. Due to the low concentration of BP-3, i.e., the value of $K_{L\text{-}H}$ C is << 1, the photocatalytic degradation of BP-3 can be simplified to the common pseudo-first-order kinetics equation (Eq. (4)) shown below [49]:

$$-\frac{dC}{dt} = k_{L\text{-}H}K_{L\text{-}H}C = k_{app}C \tag{4}$$

where k_{app} (h^{-1}) is the apparent photocatalytic rate constant or pseudo-first-order rate constant. This constant can be determined from the slope of -ln (C_t/C_0) versus the irradiation time plot (Fig. 7b), in which C_0 is the initial concentration of BP-3 in the aqueous solution at time zero and C_t is the concentration of BP-3 at irradiation time t (h). The apparent photocatalytic rate constants of different photocatalysts for the degradation of BP-3 are summarized in Fig. 7b. Accordingly, the highest k_{app} is found with

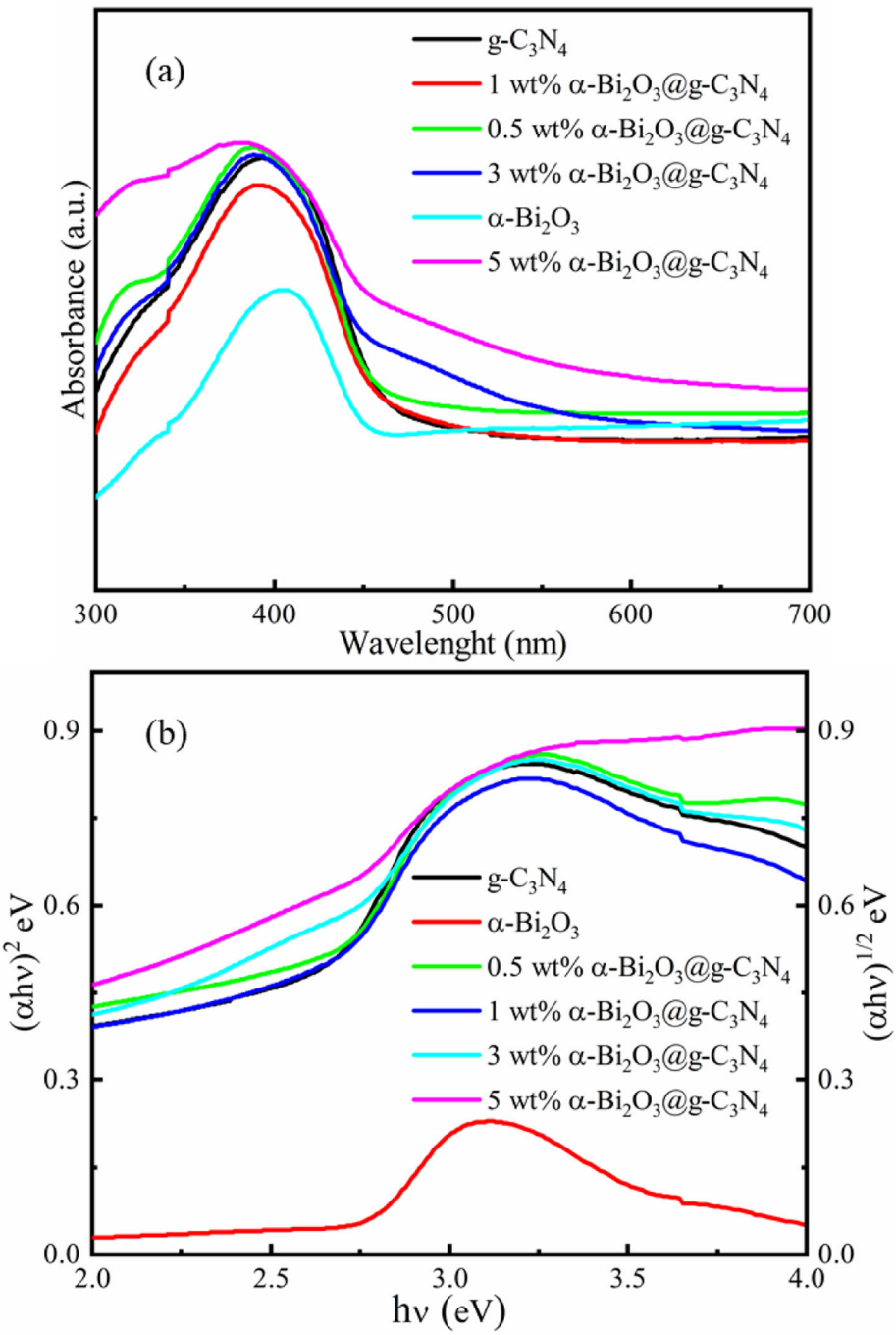

Fig. 6 (**a**) UV-vis DRS spectra and (**b**) Transformed Kubelka-Munk functions of g-C_3N_4, α-Bi_2O_3 and the α-Bi_2O_3@g-C_3N_4 composites

1 wt% α-Bi_2O_3@g-C_3N_4. The synergistic effect between the binary phases in 1 wt% α-Bi_2O_3@g-C_3N_4 results in better photogenerated electron-hole (e^--h^+) charge separation, thus inhibiting e^- and h^+ recombination.

3.4 PL and EIS spectral analysis

To examine the recombination processes of the photoinduced e^- and h^+ of the as-synthesized photocatalysts, PL spectroscopy was employed, and the spectra are shown in Fig. 8a. Herein, the PL spectra of bare g-C_3N_4, α-Bi_2O_3 and the α-Bi_2O_3@g-C_3N_4 composites were obtained with an excitation wavelength of 300 nm (~4.08 eV) to elucidate the recombination processes of the photogenerated e^--h^+ pairs. As shown in Fig. 8a, pristine g-C_3N_4 has the highest PL peak intensity, which is due to its faster rate of e^--h^+ recombination; therefore, it

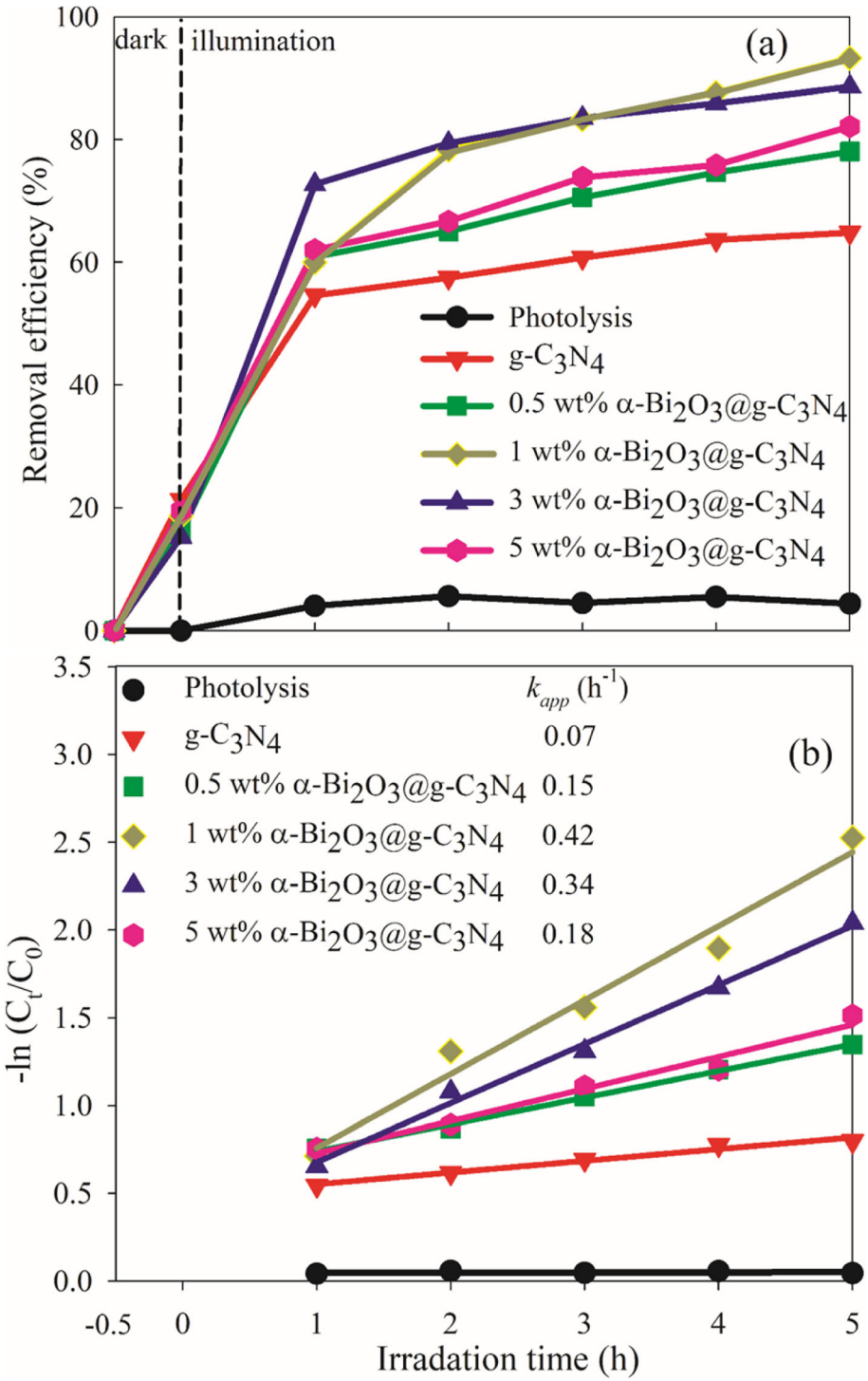

Fig. 7 (**a**) BP-3 removal efficiency achieved with pristine g-C_3N_4 and α-Bi_2O_3@g-C_3N_4 (**b**) Pseudo-first-order kinetic plots of g-C_3N_4 and the α-Bi_2O_3@g-C_3N_4 composites along with the apparent photocatalytic rate constants

shows the lowest photocatalytic activity [50]. The PL intensity of bare α-Bi_2O_3 is the lowest and is almost negligible. Hence, the PL peak intensity of the composite is lower than that of pristine g-C_3N_4, which confirms the formation of heterojunctions and indicates efficient charge separation from the CB of g-C_3N_4 to the CB of the α-Bi_2O_3 nanocluster. Therefore, the recombination process of the photoinduced charge carriers in the α-

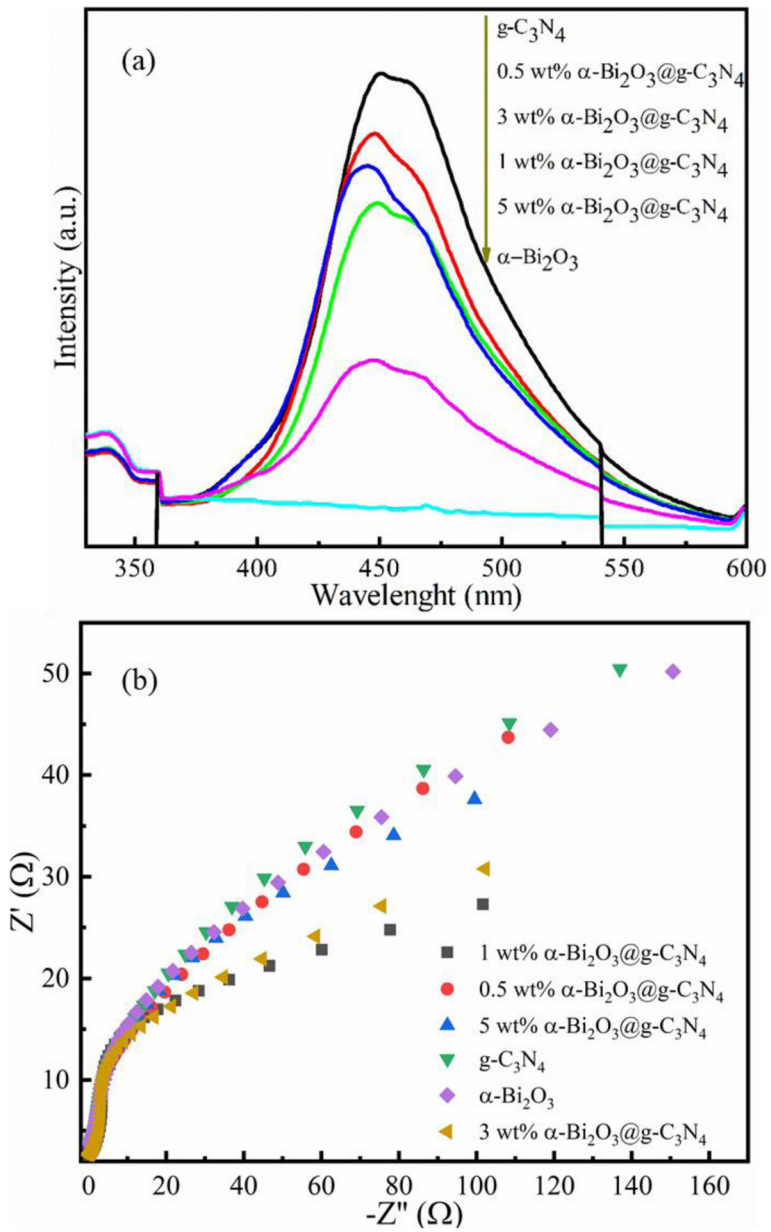

Fig. 8 (**a**) PL spectra and (**b**) EIS plots of the as-synthesized samples

Bi_2O_3@g-C_3N_4 composites is significantly hampered, which might be favorable for improving the photocatalytic activity of the composites [41].

To further demonstrate the photoinduced charge transfer efficiency and recombination processes of the as-synthesized catalysts, EIS measurements were performed. Figure 8b shows the Nyquist impedance plots of g-C_3N_4, α-Bi_2O_3 and the α-Bi_2O_3@g-C_3N_4 composites. A smaller arc radius indicates a lower charge transfer resistance (R_t) and a more facile charge transfer process at the electrode/electrolyte interface [51]. Notably, 1 wt% α-Bi_2O_3@g-C_3N_4 exhibits a smaller arc radius than the other as-synthesized samples. This result suggests that 1 wt% α-Bi_2O_3@g-C_3N_4 has a better photoinduced charge transfer efficiency and a lower recombination rate of photoinduced charge carriers [52, 53]. This scenario could be beneficial for the photocatalytic performance of 1 wt% α-Bi_2O_3@g-C_3N_4.

3.5 Possible photocatalytic mechanisms

The CB and VB potential edge positions of semiconductor materials determine their oxidation and reduction abilities; these positions can be calculated by empirical equations (Eqs. (5) and (6)) [40]

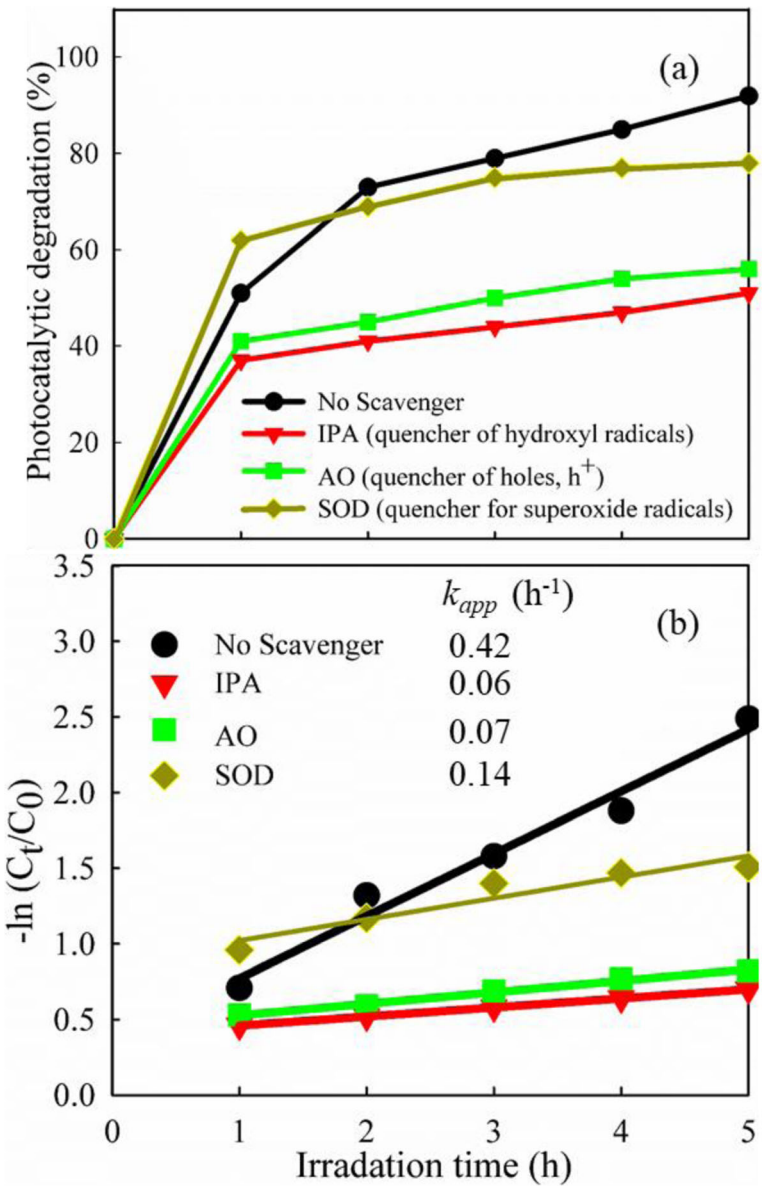

Fig. 9 (**a**) Effects of various scavengers on the degradation efficiency of 1 wt% α-Bi_2O_3@g-C_3N_4; (**b**) k_{app} of pseudo-first-order kinetics with and without scavengers

$$E_{VB} = -E^e + 0.5E_g \quad (5)$$

$$E_{CB} = E_{VB} - E_g \quad (6)$$

Herein, the E_{VB} and E_{CB} are the VB and CB potentials, respectively; x is the absolute electronegativity of the corresponding semiconductor material, which can be obtained by determining the arithmetic mean of the electron affinity and first ionization potential of the constituent atoms (5.99 eV for α-Bi_2O_3 and ~4.64 eV for g-C_3N_4) [42, 54]; E^e is the free electron energy on the hydrogen scale (~4.5 eV vs. NHE); and E_g is the bandgap energy of the semiconductors. The calculated values of the E_{VB} and E_{CB} edge positions are estimated to be ~1.50 and ~2.89 eV for the as-synthesized g-C_3N_4 and ~-1.22 and ~0.09 eV for the as-synthesized α-Bi_2O_3, respectively.

When the 1 wt% α-Bi_2O_3@g-C_3N_4 is illuminated, both g-C_3N_4 and α-Bi_2O_3 can produce a photoexcited e^--h^+ pair (Eq. (7)). The photoexcited e^- in the CB of α-Bi_2O_3 and photoinduced h^+ in the VB of g-C_3N_4 can recombine, causing the accumulation of e^- in the CB of g-C_3N_4 and h^+ in the VB of α-Bi_2O_3; this behavior results in strong oxidation and reduction for the photodegradation of BP-3 (Eq. (8)).

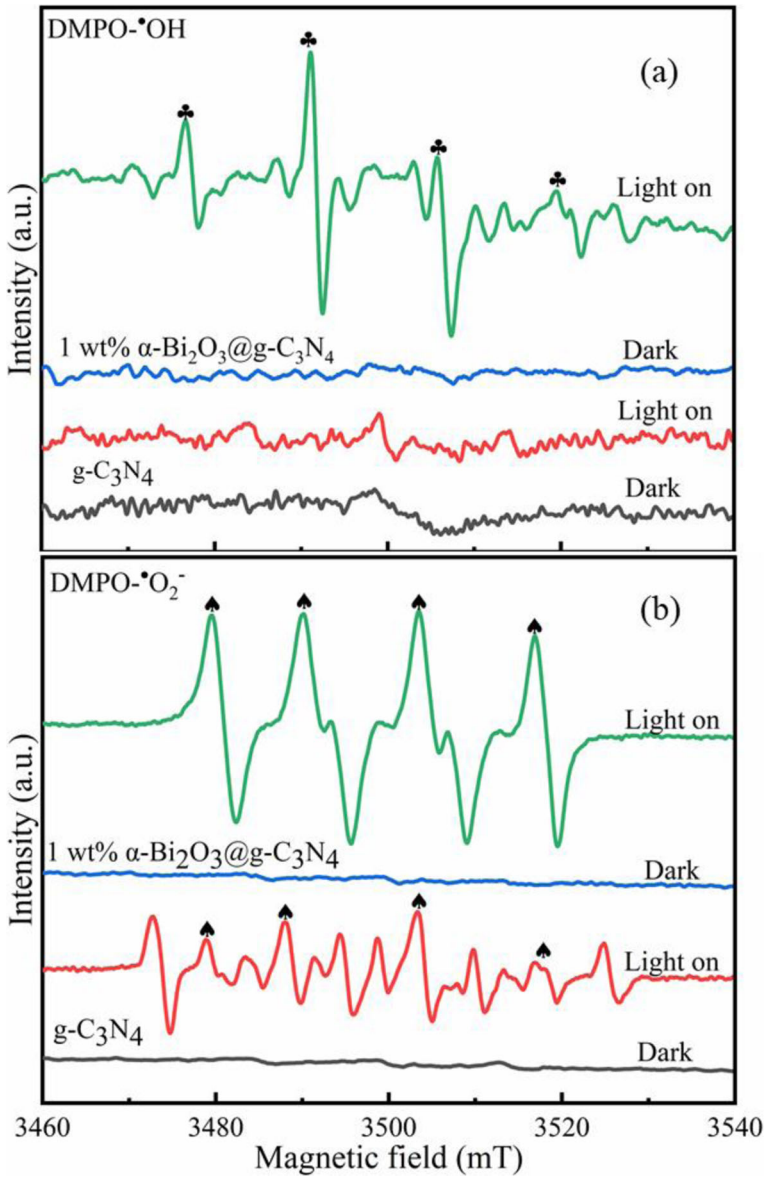

Fig. 10 EPR spectra of the (**a**) DMPO-•OH adduct in aqueous dispersion and (**b**) DMPO-$^{\bullet}O_2^-$ adduct in methanol dispersion for the 1 wt% α-Bi_2O_3@g-C_3N_4 composite and g-C_3N_4 under illumination

The reduction potential of CB in g-C_3N_4 is ~-1.22 eV vs. NHE, which is more negative than the standard redox potential of $O_2/{\bullet}O_2^-$ (~-0.33 eV vs. NHE) [55]. The photoexcited electrons in the CB of g-C_3N_4 can reduce adsorbed oxygen molecules to ${\bullet}O_2^-$ (Eq. (10)) or cause ${\bullet}O_2^-$ to react with hydrogen ions and e^- to produce H_2O_2 (Eq. (11)), which can be further reduced to generate •OH (Eq. (12)). In addition, the oxidation potential of the VB in α-Bi_2O_3 (~2.89 eV vs. NHE) is more positive than the standard redox potential of $\bullet OH/H_2O$ (~2.72 eV vs. NHE) [56]. Thus, photoinduced h^+ in the VB of α-Bi_2O_3 on the surface of the catalyst can react with H_2O to generate •OH (Eq. (9)). Additionally, the remaining h^+ in the VB of α-Bi_2O_3 on the surface of the catalyst directly oxidizes BP-3.

To further elucidate the mechanism of the photocatalytic reaction and verify the reactive species responsible for the degradation of BP-3, reactive species scavenging experiments were conducted. The results of the scavenging study with the 1 wt% α-Bi_2O_3@g-C_3N_4 composite are shown in Fig. 9. The figure shows that when IPA, AO and SOD are used as quenchers, the photodegradation rate of BP-3 decreases from 92% under normal conditions to 51, 56 and 78%, respectively, and the k_{app} for the photocatalytic degradation of BP-3 by the 1 wt% α-Bi_2O_3@g-C_3N_4 composite decreases from 0.42 h^{-1} in the

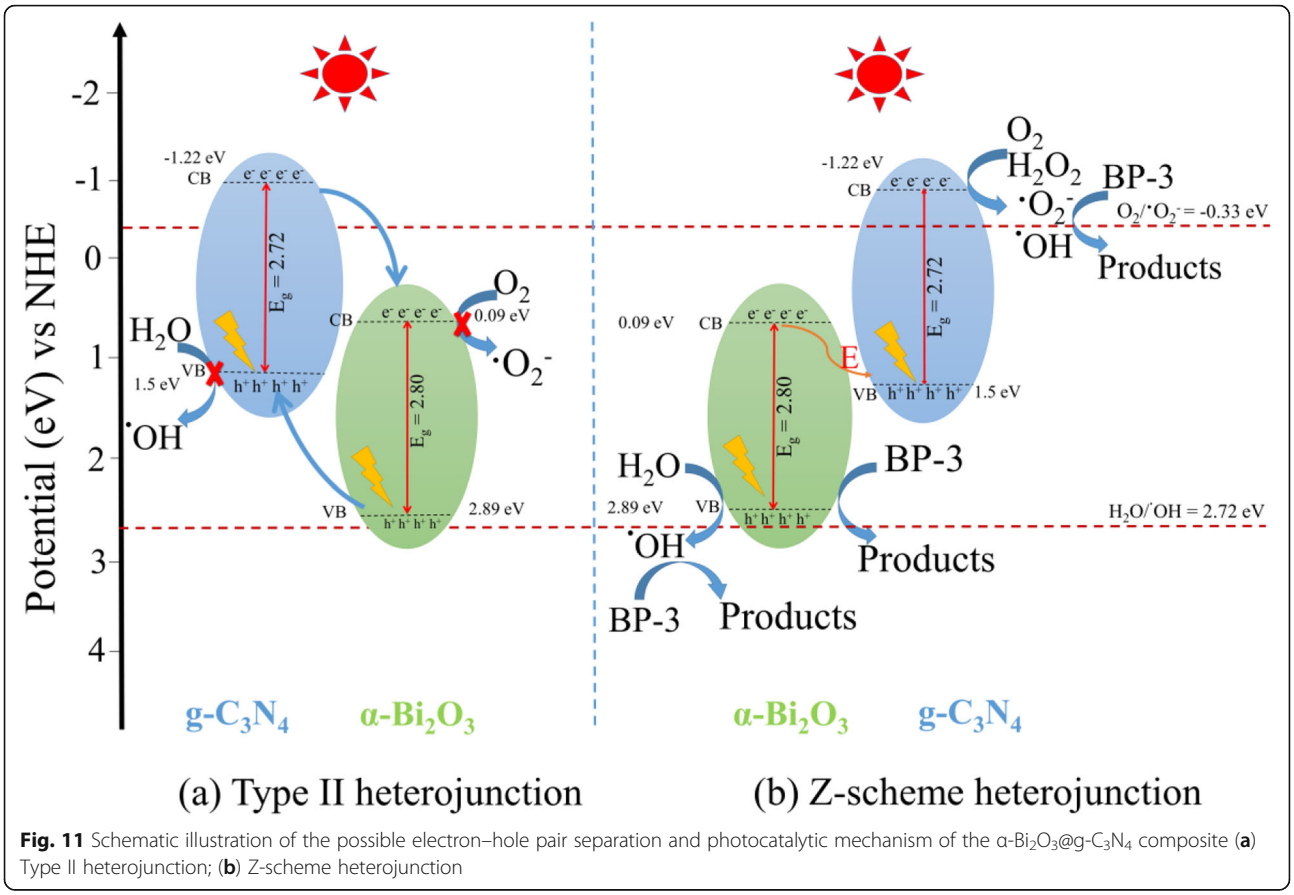

Fig. 11 Schematic illustration of the possible electron–hole pair separation and photocatalytic mechanism of the α-Bi_2O_3@g-C_3N_4 composite (**a**) Type II heterojunction; (**b**) Z-scheme heterojunction

absence of scavengers to 0.06, 0.07 and 0.14 h^{-1} in the presence of IPA, AO and SOD, respectively (Fig. 9b). Thus, the presence of IPA, AO and SOD significantly affects the photocatalytic process. Therefore, the generated •OH, h^+ and $•O_2^-$ work together to degrade BP-3 (Eq. (13)).

To ascertain the Z-scheme heterojunction and further confirm the involvement of ROS (•OH and $•O_2^-$) in the photocatalytic system, EPR measurements were performed. As depicted in Fig. 10a and b, the characteristic peaks of the •OH and $•O_2^-$ radicals were not detected prior to light exposure, whereas the typical characteristic peaks of $•O_2^-$ and •OH radicals were observed when the sample was illuminated. This result suggests that $•O_2^-$ and •OH radicals play significant roles in the photocatalytic process. As shown in Fig. 10a, the typical characteristic peak of •OH radicals for g-C_3N_4 does not appear under dark and illuminated conditions owing to the photogenerated holes on g-C_3N_4 having an inadequate oxidation potential for producing OH radicals. This result reveals that the VB potential edge of g-C_3N_4 is 1.50 eV, which is lower than the ~2.72 eV standard redox potential of •OH/H_2O. However, g-C_3N_4 can facilitate the generation of •OH radicals on the surface of 1 wt% α-Bi_2O_3@g-C_3N_4. As seen in Fig. 10b, the $•O_2^-$ EPR signal intensity of 1 wt% α-Bi_2O_3@g-C_3N_4 is stronger than that of g-C_3N_4. This result shows that more $•O_2^-$ radicals are generated on the surface of 1 wt% α-Bi_2O_3@g-C_3N_4 than on the surface of g-C_3N_4. Additionally, Figs. S12a, S13a and S14a show the 0.5 wt% α-Bi_2O_3@g-C_3N_4, 3 wt% α-Bi_2O_3@g-C_3N_4, and 5 wt% α-Bi_2O_3@g-C_3N_4 composites dispersed in methanol (for DMPO-$•O_2^-$), while Figs. S12b, S13b and S14b show the 0.5, 3, and 5 wt% α-Bi_2O_3@g-C_3N_4 composites dispersed in water (for DMPO-•OH). Thus, it can be inferred that the photocatalysis of the as-synthesized sample follows the Z-scheme photocatalytic mechanism, which not only delays charge carrier recombination but also preserves strong redox potentials to effectively degrade pollutants.

The main steps of the possible photocatalytic reaction mechanism are proposed as follows:

$$\alpha\text{–}Bi_2O_3@g\text{–}C_3N_4 + h^+ \rightarrow \alpha\text{–}Bi_2O_3\left(e^- + h^+\right) + g\text{–}C_3N_4\left(e^- + h^+\right) \quad (7)$$

$$\alpha\text{–}Bi_2O_3\left(e^- + h^+\right) + g\text{–}C_3N_4\left(e^- + h^+\right) \rightarrow \alpha\text{–}Bi_2O_3\left(h^+\right) + g\text{–}C_3N_4\left(e^-\right) \quad (8)$$

$$2h^+ + 2H_2O \rightarrow 2•OH + 2H^+ \quad (9)$$

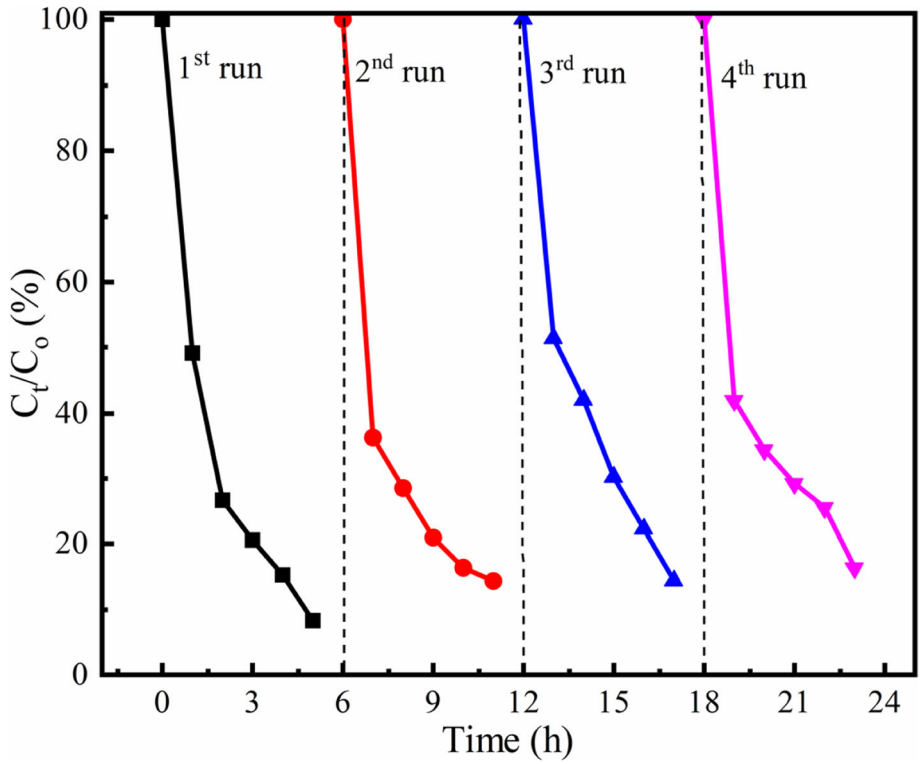

Fig. 12 Reusability test of the 1 wt% α-Bi_2O_3@g-C_3N_4 composite

$$O_{2\ (ads)} + e^- \rightarrow 2\bullet O_2^- \quad (10)$$

$$2\bullet O_2^- + 2H^+ + e^- \rightarrow H_2O_2 \quad (11)$$

$$H_2O_2 + e^- \rightarrow \bullet OH + OH^- \quad (12)$$

$$h^+, \bullet O_2^- \& \bullet OH + BP{-}3 \rightarrow \text{Intermediate product} \rightarrow CO_2 + H_2O \quad (13)$$

From the obtained experimental and characterization results, a schematic illustration showing the possible photodegradation mechanism is proposed in Fig. 11.

To further confirm the photodegradation of BP-3, HPLC measurements were conducted. Figure S10d shows the HPLC chromatograms of BP-3 before and after photocatalytic degradation by the 1 wt% α-Bi_2O_3@g-C_3N_4 composite. The flow rate was 0.8 mL min^{-1}, and the injection volume was 20 μL. Two major peaks are recorded for the 300 min photocatalytic degradation process. The peaks centered at 4.68 and 8.21 min correspond to BP-3 and an intermediate byproduct, respectively. The peak intensities of BP-3 and the intermediate byproduct significantly decrease during the photodegradation process, which indicates that both BP-3 and the intermediate byproducts degrade during photocatalysis. Generally, BP-3 is metabolized to 2,4-dihydroxybenzophenone and dioxybenzone via demethylation and hydroxylation routes, respectively [18].

3.6 Photocatalyst reusability test

The reusability of catalysts is a very important parameter for their practical application. Herein, we investigated the reusability of the as-synthesized 1 wt% α-Bi_2O_3@g-C_3N_4 by performing four successive recycling runs, and the results are shown in Fig. 12. The removal efficiencies observed after the second, third and fourth recycling runs for BP-3 photodegradation decrease slightly by 4%, 6% and 8%, respectively. This decrease might be due to the loss of some catalyst during the washing, centrifugation and drying procedures and the active sites of the catalyst surface being covered by reactive chemicals. However, the apparent rate constant of 1 wt% α-Bi_2O_3@g-C_3N_4 after the fourth recycling test indicated a higher photocatalytic efficiency than that after the other runs. Therefore, the as-synthesized 1 wt% α-Bi_2O_3@g-C_3N_4 has good stability and favorable reusability, which promotes its practical applicability.

4 Conclusions

In this study, novel α-Bi_2O_3@g-C_3N_4 composites with different weight percentages (0.5, 1, 3 and 5 wt%) of α-Bi_2O_3 were synthesized by a mixing-calcination strategy. Among these photocatalysts, 1 wt% α-Bi_2O_3@g-C_3N_4 showed higher photocatalytic efficiency than the other photocatalysts for BP-3 degradation, exhibiting an optimal rate constant of 0.42 h^{-1}, which is up to 6.3 times

higher than that of pristine g-C_3N_4. The improved photocatalytic performance can be attributed mainly to the enhanced photogenerated e^--h^+ charge separation and suppressed e^- and h^+ recombination, which are dominant factors for improving the photocatalytic activity. More importantly, radical trapping experiments and EPR findings confirm that the active species •OH, h^+ and $•O^{2-}$ work together to enhance the photocatalytic activity of the composite. The migration pattern of photogenerated carriers suggests a Z-scheme photocatalytic mechanism rather than a type II mechanism. The method presented in this study might be considered a promising approach for the removal of emerging organic pollutants.

5 Supplementary Information

The online version contains supplementary material available at https://doi.org/10.1186/s42834-022-00129-8.

Additional file 1. Supplementary materials.

Acknowledgments

This work was supported by the Ministry of Science and Technology of Taiwan (MOST 108-2621-M-010-002). The authors are grateful to the Electron Microscopy Facility at National Yang Ming Chiao Tung University for providing the TEM, SEM and EDS images. They are also grateful to the National Taiwan University of Science and Technology for providing the XRD and XPS measurements. We also appreciate the EIS and measurements provided by National Tsing Hua University (NTHU) and the BET and BJH data obtained from the facility at National Chung Hsing University. The authors would like to thank the Instrumentation Center at NTHU for providing the EPR measurement.

Authors' contributions

Abiyu Kerebo Berekute conducted the experiments and wrote the study. Kuo-Pin Yu and Yi-Hsueh Brad Chuang are Abiyu Kerebo Berekute's advisor and coadvisor, respectively. They provided research ideas and guidance for this study. All authors read and approved the final manuscript.

Funding

This work was supported by the Ministry of Science and Technology of Taiwan (MOST 108-2621-M-010-002).

Availability of data and materials

All data generated or analyzed during this study are available within the article and Supplementary Materials.

Declarations

Competing interests

The authors declare they have no competing interests.

Author details

[1]International Ph.D Program in Environmental Science and Technology, University System of Taiwan, Taipei 11221, Taiwan. [2]Institute of Environmental and Occupational Health Sciences, National Yang Ming Chiao Tung University, Taipei 11221, Taiwan. [3]Institute of Environmental Engineering, National Yang Ming Chiao Tung University, Hsinchu City 30010, Taiwan.

Received: 12 July 2021 Accepted: 23 February 2022
Published online: 14 March 2022

References

1. Diaz-Cruz MS, Molins-Delgado D, Serra-Roig MP, Kalogianni E, Skoulikidis NT, Barcelo D. Personal care products reconnaissance in EVROTAS river (Greece): water-sediment partition and bioaccumulation in fish. Sci Total Environ. 2019;651:3079–89.
2. Molins-Delgado D, Diaz-Cruz MS, Barcelo D. Ecological risk assessment associated to the removal of endocrine-disrupting parabens and benzophenone-4 in wastewater treatment. J Hazard Mater. 2016;310:143–51.
3. Zhao L, Deng JH, Sun PZ, Liu JS, Ji Y, Nakada N, et al. Nanomaterials for treating emerging contaminants in water by adsorption and photocatalysis: systematic review and bibliometric analysis. Sci Total Environ. 2018;627:1253–63.
4. Mao FJ, He YL, Gin KYH. Occurrence and fate of benzophenone-type UV filters in aquatic environments: a review. Environ Sci-Wat Res. 2019;5:209–23.
5. Xue YC, Dong WB, Wang XN, Bi WL, Zhai PP, Li HJ, et al. Degradation of sunscreen agent p-aminobenzoic acid using a combination system of UV irradiation, persulphate and iron (II). Environ Sci Pollut R. 2016;23:4561–8.
6. Peng MG, Li HJ, Du ED, Feng HQ, Wang JL, Li DD, et al. OH-initiated oxidation mechanism and kinetics of organic sunscreen benzophenone-3: a theoretical study. Chem Pap. 2016;70:856–68.
7. Liu YS, Ying GG, Shareef A, Kookana RS. Occurrence and removal of benzotriazoles and ultraviolet filters in a municipal wastewater treatment plant. Environ Pollut. 2012;165:225–32.
8. Wick A, Marincas O, Moldovan Z, Ternes TA. Sorption of biocides, triazine and phenylurea herbicides, and UV-filters onto secondary sludge. Water Res. 2011;45:3638–52.
9. Langford KH, Reid MJ, Fjeld E, Oxnevad S, Thomas KV. Environmental occurrence and risk of organic UV filters and stabilizers in multiple matrices in Norway. Environ Int. 2015;80:1–7.
10. Li WH, Ma YM, Guo CS, Hu W, Liu KM, Wang YQ, et al. Occurrence and behavior of four of the most used sunscreen UV filters in a wastewater reclamation plant. Water Res. 2007;41:3506–12.
11. Tsui MMP, Leung HW, Lam PKS, Murphy MB. Seasonal occurrence, removal efficiencies and preliminary risk assessment of multiple classes of organic UV filters in wastewater treatment plants. Water Res. 2014;53:58–67.
12. Garcia-Segura S, Brillas E. Applied photoelectrocatalysis on the degradation of organic pollutants in wastewaters. J Photoch Photobio C. 2017;31:1–35.
13. Ghasemian S, Nasuhoglu D, Omanovic S, Yargeau V. Photoelectrocatalytic degradation of pharmaceutical carbamazepine using Sb-doped Sn-80%-W-20%-oxide electrodes. Sep Purif Technol. 2017;188:52–9.
14. Shao BB, Liu XJ, Liu Z, Zeng GM, Liang QH, Liang C, et al. A novel double Z-scheme photocatalyst $Ag_3PO_4/Bi_2S_3/Bi_2O_3$ with enhanced visible-light photocatalytic performance for antibiotic degradation. Chem Eng J. 2019;368:730–45.
15. Aslam M, Ismail IMI, Chandrasekaran S, Hameed A. Morphology controlled bulk synthesis of disc-shaped WO_3 powder and evaluation of its photocatalytic activity for the degradation of phenols. J Hazard Mater. 2014;276:120–8.
16. Liu N, Lu N, Su Y, Wang P, Quan X. Fabrication of g-C_3N_4/Ti_3C_2 composite and its visible-light photocatalytic capability for ciprofloxacin degradation. Sep Purif Technol. 2019;211:782–9.
17. Wang Z, Deb A, Srivastava V, Iftekhar S, Arnbat I, Sillanpaa M. Investigation of textural properties and photocatalytic activity of PbO/TiO_2 and Sb_2O_3/TiO_2 towards the photocatalytic degradation Benzophenone-3 UV filter. Sep Purif Technol. 2019;228:115763.
18. Zuniga-Benitez H, Aristizabal-Ciro C, Penuela GA. Heterogeneous photocatalytic degradation of the endocrine-disrupting chemical Benzophenone-3: parameters optimization and by-products identification. J Environ Manage. 2016;167:246–58.
19. Zhu WY, Sun FQ, Goei R, Zhou Y. Construction of WO_3-g-C_3N_4 composites as efficient photocatalysts for pharmaceutical degradation under visible light. Catal Sci Technol. 2017;7:2591–600.
20. Ismael M, Wu Y. A facile synthesis method for fabrication of $LaFeO_3$/g-C_3N_4 nanocomposite as efficient visible-light-driven photocatalyst for photodegradation of RhB and 4-CP. New J Chem. 2019;43:13783–93.
21. Wang XX, Zhang LH, Lin HJ, Nong QY, Wu Y, Wu TH, et al. Synthesis and characterization of a ZrO_2/g-C_3N_4 composite with enhanced visible-light photoactivity for rhodamine degradation. RSC Adv 2014;4:40029–35.

22. Li HF, Ma AQ, Zhang D, Gao YQ, Dong YH. Rational design direct Z-scheme BiOBr/g-C_3N_4 heterojunction with enhanced visible photocatalytic activity for organic pollutants elimination. RSC Adv. 2020;10:4681–9.
23. Zhang LP, Wang GH, Xiong ZZ, Tang H, Jiang CJ. Fabrication of flower-like direct Z-scheme β-Bi_2O_3/g-C_3N_4 photocatalyst with enhanced visible light photoactivity for Rhodamine B degradation. Appl Surf Sci. 2018;436:162–71.
24. Peng H, Guo RT, Lin H, Liu XY. Synthesis of Bi_2O_3/g-C_3N_4 for enhanced photocatalytic CO_2 reduction with a Z-scheme mechanism. RSC Adv. 2019;9:37162–70.
25. Li HJ, Tu WG, Zhou Y, Zou ZG. Z-scheme photocatalytic systems for promoting photocatalytic performance: recent progress and future challenges. Adv Sci. 2016;3:1500389.
26. Xu QL, Zhang LY, Cheng B, Fan JJ, Yu JG. S-scheme heterojunction photocatalyst. Chem-US. 2020;6:1543–59.
27. Cui YQ, Nengzi LC, Gou JF, Huang Y, Li B, Cheng XW. Fabrication of dual Z-scheme MIL-53(Fe)/α-Bi_2O_3/g-C_3N_4 ternary composite with enhanced visible light photocatalytic performance. Sep Purif Technol. 2020;232:115959.
28. Xue JW, Bao J. Interfacial charge transfer of heterojunction photocatalysts: characterization and calculation. Surf Interfaces. 2021;25:101265.
29. Ghosh U, Pal A. Graphitic carbon nitride based Z scheme photocatalysts: design considerations, synthesis, characterization and applications. J Ind Eng Chem. 2019;79:383–408.
30. Zhang ZY, Jiang DL, Xing CS, Chen LL, Chen M, He MQ. Novel AgI-decorated β-Bi_2O_3 nanosheet heterostructured Z-scheme photocatalysts for efficient degradation of organic pollutants with enhanced performance. Dalton T. 2015;44:11582–91.
31. Li YJ, Yang F, Yu Y. Enhanced photocatalytic activity of α-Bi_2O_3 with high electron-hole mobility by codoping approach: a first-principles study. Appl Surf Sci. 2015;358:449–56.
32. Ge L, Han CC, Liu J. Novel visible light-induced g-C_3N_4/Bi_2WO_6 composite photocatalysts for efficient degradation of methyl orange. Appl Catal B-Environ. 2011;108–9:100–7.
33. Lu HJ, Hao Q, Chen T, Zhang LH, Chen DM, Ma C, et al. A high-performance Bi_2O_3/Bi_2SiO_5 p-n heterojunction photocatalyst induced by phase transition of Bi_2O_3. Appl Catal B-Environ. 2018;237:59–67.
34. Liu SL, Chen JL, Xu DF, Zhang XC, Shen MY. Enhanced photocatalytic activity of direct Z-scheme Bi_2O_3/g-C_3N_4 composites via facile one-step fabrication. J Mater Res. 2018;33:1391–400.
35. Zhang JF, Hu YF, Jiang XL, Chen SF, Meng SG, Fu XL. Design of a direct Z-scheme photocatalyst: preparation and characterization of Bi_2O_3/g-C_3N_4 with high visible light activity. J Hazard Mater. 2014;280:713–22.
36. Cao L, Wang R, Wang DX. Synthesis and characterization of sulfur self-doped g-C_3N_4 with efficient visible-light photocatalytic activity. Mater Lett. 2015;149:50–3.
37. Chen DD, Wu SX, Fang JZ, Lu SY, Zhou GY, Feng WH, et al. A nanosheet-like α-Bi_2O_3/g-C_3N_4 heterostructure modified by plasmonic metallic Bi and oxygen vacancies with high photodegradation activity of organic pollutants. Sep Purif Technol. 2018;193:232–41.
38. He RA, Zhou JQ, Fu HQ, Zhang SY, Jiang CJ. Room-temperature in situ fabrication of Bi_2O_3/g-C_3N_4 direct Z-scheme photocatalyst with enhanced photocatalytic activity. Appl Surf Sci. 2018;430:273–82.
39. Liu W, Zhou JB, Zhou J. Facile fabrication of multi-walled carbon nanotubes (MWCNTs)/ α-Bi_2O_3 nanosheets composite with enhanced photocatalytic activity for doxycycline degradation under visible light irradiation. J Mater Sci. 2019;54:3294–308.
40. Liu W, Zhou JB, Hu ZS, Zhou J, Cai WQ. In situ facile fabrication of Z-scheme leaf-like β-Bi_2O_3/g-C_3N_4 nanosheets composites with enhanced visible light photoactivity. J Mater Sci-Mater El. 2018;29:14906–17.
41. Tian N, Huang HW, Guo YX, He Y, Zhang YH. A g-C_3N_4/$Bi_2O_2CO_3$ composite with high visible-light-driven photocatalytic activity for rhodamine B degradation. Appl Surf Sci. 2014;322:249–54.
42. Li YP, Wu SL, Huang LY, Xu H, Zhang RX, Qu ML, et al. g-C_3N_4 modified Bi_2O_3 composites with enhanced visible-light photocatalytic activity. J Phys Chem Solids. 2015;76:112–9.
43. Huang LY, Li YP, Xu H, Xu YG, Xia JX, Wang K, et al. Synthesis and characterization of CeO_2/g-C_3N_4 composites with enhanced visible-light photocatalytic activity. RSC Adv. 2013;3:22269–79.
44. Wang K, Li Q, Liu BS, Cheng B, Ho WK, Yu JG. Sulfur-doped g-C_3N_4 with enhanced photocatalytic CO_2-reduction performance. Appl Catal B-Environ. 2015;176:44–52.
45. Zhan S, Zhou F, Huang NB, Yang YF, Liu YJ, Yin YF, et al. g-C_3N_4/$ZnWO_4$ films: preparation and its enhanced photocatalytic decomposition of phenol in UV. Appl Surf Sci. 2015;358:328–35.
46. Zhang JH, Qian HY, Liu WC, Chen H, Qu Y, Lin ZD. The construction of the heterostructural Bi_2O_3/g-C_3N_4 composites with an enhanced photocatalytic activity. Nano. 2018;13:1850063.
47. Deng YC, Tang L, Zeng GM, Wang JJ, Zhou YY, Wang JJ, et al. Facile fabrication of a direct Z-scheme Ag_2CrO_4/g-C_3N_4 photocatalyst with enhanced visible light photocatalytic activity. J Mol Catal A-Chem. 2016;421:209–21.
48. Cantrell A, McGarvey DJ, George Truscott TG. Photochemical and photophysical properties of sunscreens. In: Giacomoni PU, editor. Comprehensive series in photosciences. Amsterdam: Elsevier; 2001. p. 497–519.
49. Padhiari S, Hota G. A Ag nanoparticle functionalized Sg-C_3N_4/Bi_2O_3 2D nanohybrid: a promising visible light harnessing photocatalyst towards degradation of rhodamine B and tetracycline. Nanoscale Adv. 2019;1:3212–24.
50. Kumar A, Kumar S, Bahuguna A, Kumar A, Sharma V, Krishnan V. Recyclable, bifunctional composites of perovskite type N-$CaTiO_3$ and reduced graphene oxide as an efficient adsorptive photocatalyst for environmental remediation. Mater Chem Front. 2017;1:2391–404.
51. Cui YQ, Zhang XY, Guo RN, Zhang HX, Li B, Xie MZ, et al. Construction of Bi_2O_3/g-C_3N_4 composite photocatalyst and its enhanced visible light photocatalytic performance and mechanism. Sep Purif Technol. 2018;203:301–9.
52. Orimolade BO, Arotiba OA. Towards visible light driven photoelectrocatalysis for water treatment: application of a FTO/$BiVO_4$/Ag_2S heterojunction anode for the removal of emerging pharmaceutical pollutants. Sci Rep-UK. 2020;10:5348.
53. Tadesse SF, Kuo DH, Kebede WL, Duresa LW. Synthesis and characterization of vanadium-doped $Mo(O,S)_2$ oxysulfide for efficient photocatalytic degradation of organic dyes. New J Chem. 2020;44:19868–79.
54. Koci K, Reli M, Troppova I, Sihor M, Kupkova J, Kustrowski P, et al. Photocatalytic decomposition of N_2O over TiO_2/g-C_3N_4 photocatalysts heterojunction. Appl Surf Sci. 2017;396:1685–95.
55. Habibi-Yangjeh A, Akhundi A. Novel ternary g-C_3N_4/Fe_3O_4/Ag_2CrO_4 nanocomposites: magnetically separable and visible-light-driven photocatalysts for degradation of water pollutants. J Mol Catal A-Chem. 2016;415:122–30.
56. Hong YZ, Jiang YH, Li CS, Fan WQ, Yan X, Yan M, et al. In-situ synthesis of direct solid-state Z-scheme V_2O_5/g-C_3N_4 heterojunctions with enhanced visible light efficiency in photocatalytic degradation of pollutants. Appl Catal B-Environ. 2016;180:663–73.

Publisher's Note